Nanoscale

PAPER

View Article Online
View Journal

Cite this: DOI: 10.1039/d5nr05002b

Mass spectral molecular mapping shows benefits of thermal evaporation in prelithiated silicon-based electrodes

Gabriel D. Parker, [a] Amanda L. Musgrove, [b] Gabriel M. Veith, [b] Ivan Matyushov [a] and Xiao-Ying Yu *[a]

Silicon based composites have become increasingly popular as potential anodes for lithium-ion batteries due to their large storage capacity and potential ability to generate batteries with energy densities greater than 350 Wh kg^{-1}. These anodes often see reduced initial columbic efficiency (ICE) due to disruptive volume expansionup to 300% and continuous solid electrolyte interphase (SEI) layer formation. Prelithiation, where an excess reservoir of Li is added to the electrode to compensate for irreversible SEI formation losses during their sample preparation, has proven to solve the issue of immediate capacity loss. Thermal evaporation is a prelithiation technique with limited studies on its effectiveness. In this study, time-of-flight secondary ion mass spectrometry (ToF-SIMS) is used to highlight the benefits of prelithiation *via* thermal evaporation. ToF-SIMS provides chemical mapping and spatial information in 2D and 3D visualizing the deposition of lithium, identifying Li_xSi_y alloy and $Li_xSi_yO_z$ silicate formation, and the distribution of lithium passivation into the electrodes. Passivation under different atmospheric conditions, such as inert Argon (Ar) and Ar/ carbon dioxide (CO_2), highlights the impact of the environment on the passivation effectiveness and formation of Li_xSi_y alloy and $Li_xSi_yO_z$ silicate. The ToF-SIMS molecular imaging and depth profiling results indicate that prelithiation *via* thermal evaporation effectively distributes lithium throughout the depth profile thickness of several hundred nanometers. It induces a greater degree of $Li_xSi_yO_z$ silicate formation over Li_xSi_y alloy. Our ToF-SIMS characterization results show the effectiveness of thermal evaporation in producing a more stable electrode and an electrode with an effective lithium reserve that can preserve its capacity.

Received 26th November 2025,
Accepted 8th April 2026

DOI: 10.1039/d5nr05002b

rsc.li/nanoscale

Introduction

Lithium-ion batteries (LIBs) are the most developed, widely used energy storage technology across the globe. Improving their capacity, stability, and safety is crucial to expanding their applications and functionality. Traditional LIBs with graphite anodes are matured technologies that demand sophisticated engineering of graphite or the use of alternative materials to meet future energy storage demands.[1–3] Silicon-based anodes are promising alternatives to graphite due to silicon's significantly larger specific energy capacity (up to 4200 mAh g^{-1}) compared to graphite,[4] relative abundance, and low cost.[2] However, silicon's large volume swings (~300%)[5] leads to the formation of an unstable solid electrolyte interphase (SEI). These swings lower the structural integrity of the anode, leading to immediate and permanent loss of lithium (as measure by capacity) and initial coulombic efficiencies (ICE).[6] Silicon's sudden capacity loss when cycling is a crucial detriment to its widespread use as an anode material.

Prelithiation, where lithium-containing material is added to an anode during its sample preparation, is a promising processing method to counteract the capacity and ICE loss during cycling of silicon-based electrodes.[7] Currently, a prelithiation method suitable for use in manufacturing and commercializing silicon-based anodes has yet to be found. Various prelithiation methods have been developed and tested such as prelithiation of the binder,[8–11] electrochemical prelithiation,[12–15] chemical prelithiation,[16–23] and direct contact prelithiation.[24–34] A new approach is prelithiation *via* thermal evaporation.[35–37] Here, a lithium metal source is evaporated onto the anode where the lithium accumulates on the surface and diffuses throughout the anode forming lithium–silicon alloys through solid state diffusion. Thermal evaporation is quick, easy to control, and has been shown to be more uniform along with producing a greater discharge capacity compared to direct contact prelithiation.[36] However, prelithiation *via* thermal evaporation alone still fails to deter the excess volumetric expansion of silicon-based

[a]*Materials Science and Technology Division, Oak Ridge National Laboratory, Oak Ridge, TN 37830, USA. E-mail: yuxiaoying@ornl.gov*
[b]*Chemical Sciences Division, Oak Ridge National Laboratory, Oak Ridge, TN 37830, USA*

anodes or the eventual losses of lithium inventory due to deleterious side reactions.[36,37]

A recently published article covering the thermal evaporation of lithium as a prelithiation technique for silicon-based composites was explored.[37] Uniquely, a fine steel mesh covered the sample electrodes to reduce the strain and volumetric expansion during prelithiation by confining the lithium to deposit in 'islands'. It was reported that the prelithiated anodes have higher initial coulombic efficiency, but their capacity fade is faster compared to their non-prelithiated samples due to the increased use of silicon and alloy formation that strains the electrodes.

Prelithiation is known to alleviate the problem of reduced ICE in silicon-based anodes, but it also exacerbates the formation of unstable, reactive Li_xSi_y alloy products.[33,34,38,39] Not only does this alloy render the electrodes unsuitable for ambient conditions,[33] but specific alloy phases, like $Li_{15}Si_4$, create internal stress that reduce the electrodes' structural and cycling stability.[38,39] Lessening Li_xSi_y alloy presence and instead increasing $Li_xSi_yO_z$ silicate growth is found to improve the capacity and efficiency of silicon-based anodes.[33,34] $Li_xSi_yO_z$ silicates bring about more air stability,[33] moderate volume expansion, and provide more mechanical strength to silicon-based electrodes.[38]

Time-of-flight secondary ion mass spectrometry (ToF-SIMS) is a highly sensitive surface analysis technique known for its low mass deviation and high lateral resolution.[40] Unlike other surface techniques, such as X-ray photoelectron spectroscopy and scanning electron microscopy, ToF-SIMS offers both molecular and two-dimensional (2D)/ three-dimensional (3D) chemical distributional imaging.[41,42] Other mass spectrometral imaging approaches, such as matrix assisted laser desorption ionization mass spectrometry (MALDI-MS) and differential electrochemical mass spectrometry (DEMS), have been used to study SEI; however, they are limited to the supermicrometer spatial resolutions when compared to SIMS. For instance, MALDI-MS typically obtains information regarding polymeric additives of the SEI and DEMS obtains gas evolution information.[43,44] ToF-SIMS is the dominant surface analysis technique used in this study to substantiate the effectiveness of prelithiation *via* thermal evaporation. ToF-SIMS high sensitivity to detect lithium ions and interphase compounds in addition to its mass spectrometry, depth profiling, surface imaging, and 3D imaging capabilities make it particularly effective at analysing lithiation dynamics.[45,46] ToF-SIMS is commonly used for studying cycled electrodes. It has not been used for analysis of prelithiation processes to the best of our knowledge.

Here, ToF-SIMS analysis was performed on composite anodes consisting of silicon, polyimide, and carbon black that were prelithiated *via* thermal evaporation. Depth profiles, 2D/ 3D molecular images, and high resolution mass spectra were collected to map out Li arrangement on the surface, evaluate the dispersion of Li, and identify the presence of key Li_xSi_y and $Li_xSi_yO_z$ compounds. This new application of ToF-SIMS validates the effectiveness of the unique prelithiation method.

Methods

Preparation of electrodes

Detailed sample preparation can be found elsewhere.[37] In brief, silicon composite anodes constructed from 80 : 10 : 10 wt% Si : polyimide (P84) : carbon black slurries where silicon is the primary anode material, P84 is the binder, and carbon black acts to enhance the samples' conductivity and as a rheological aid. The silicon was formed by milling silicon chunks in propylene carbonate and the resulting material is oxide terminated. 1-Methyl-2-pyrrolidinone (NMP) was added to the slurry and mixed using a Turbula mixer for 1 hour. This slurry was then doctorbladed onto a Cu foil current collector with a 100 μm wet gap, and circular electrodes were punched out providing a 15 mm diameter, 1.77 cm^2 electrode area. The electrodes were cured at 350 °C for 1 hour under Ar. The electrodes were placed in an argon-filled glovebox under high-vacuum (>10^{-7} Torr) with a tantalum crucible containing lithium. A stainless-steel mesh was placed over the sample electrodes to deposit lithium into 'islands' or pockets on the electrodes' surface. After prelithiation, the mesh was removed to reveal a composite electrode with no surface cracking.[37] To initiate the prelithiation process, the crucible containing lithium was heated and evaporated toward the sample. For passivation, one sample electrode was placed into the vacuum chamber, where the vacuum chamber was backfilled with 96% Ar and 4% CO_2 gas environment, while the second was passivated in a high purity argon filled glove box (<1 ppm H_2O; <10 ppm O_2).

ToF-SIMS analysis

Both static and dynamic ToF-SIMS analyses were performed with an IONTOF ToF.SIMS.5-NCS instrument (IONTOF GmbH, Münster, Germany). Fig. 1 displays a schematic of the general ToF-SIMS process and equipment involved. For static ToF-SIMS, a 30 keV Bi_3^+ primary cluster ion beam and with a 0.5 pA current 10 kHz pulse rate, and ion dose density of 5.11 × 10^{10} ions per cm^2 was used. An electron flood gun was used for charge compensation. The chamber pressure was maintained at ~8.0 × 10^{-9} Torr during analysis. Static ToF-SIMS spectra were acquired over a 500 μm × 500 μm area for 60 scans with 256 × 256-pixel resolution and 100 μs cycle time. Five replicate measurements were acquired for each sample in positive and negative ion modes. Reproducibility plots can be found in Fig. S1–S3.

ToF-SIMS depth profiling was performed using an added 2 keV Cs^+ sputter ion beam with a 600 × 600 μm^2 sputter area and 300 × 300 μm^2 analysis area. Non-interlaced mode was used with 10 s sputter time and one analysis frame per scan with a 256 × 256-pixel resolution. A total of 250 scans were collected. Results from the negative ion mode are presented to study the lithium distributions and verify the presence of lithium–silicon compounds and passivation layers. The results presented herein include high mass resolution mass spectra, 2D surface images of key ions, depth profile plots, and 3D dis-

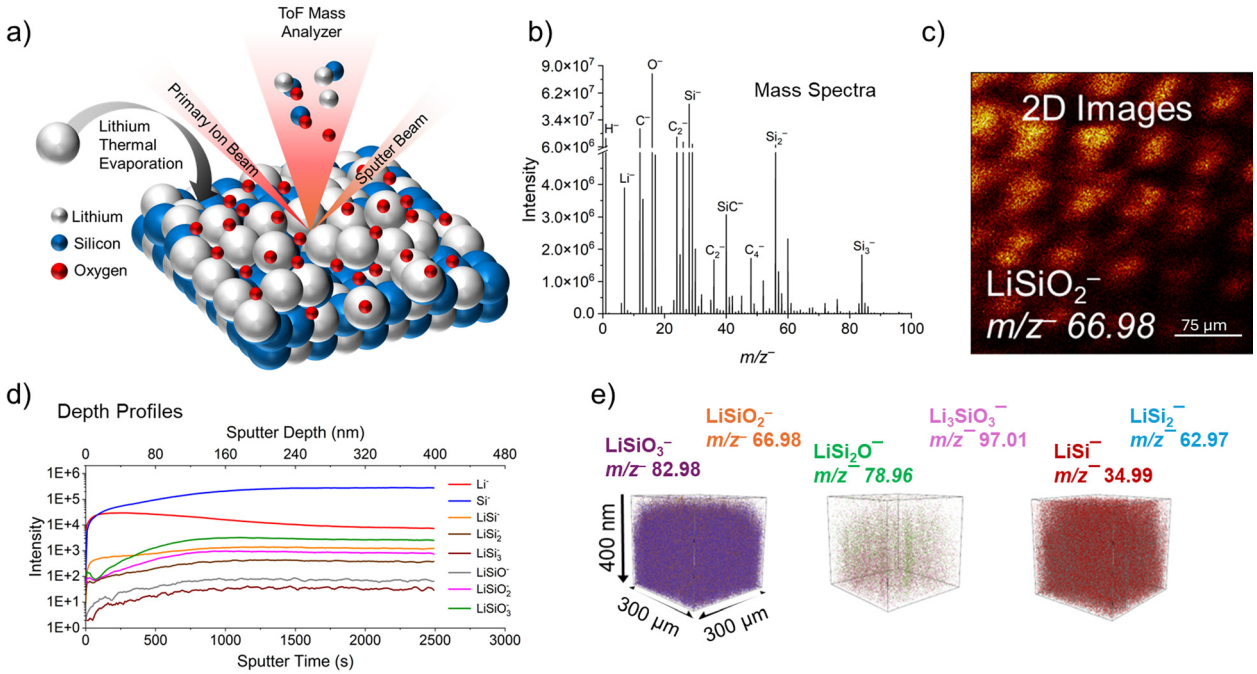

Fig. 1 ToF-SIMS schematic (a) providing overview of the battery sample highlighting the silicon anode with lithium passivation and surface oxidation identifying molecules such as Li^-, Si^-, $Li_xO_y^-$, $Li_xSi_y^-$, and $Li_xSi_yO_z^-$ molecules during analysis. ToF-SIMS collects data such as mass spectra (b), 2D images (c), depth profiles (d) and 3D reconstructions (e) showing the spatial and lateral distributions of interest analytes.

tribution images of key ions. Additional positive ion mode results are included in the SI.

ToF-SIMS images provided in this work were acquired using high mass resolution spectrometry mode, not high spatial resolution imaging mode. Mass spectroscopy mode was chosen to study surface chemistry and compositional changes into the bulk of the electrode material. It is worth noting that some ion distribution in the spectroscopy mode may not have the exact distribution as that in the high spatial imaging mode due to the inherent spatial resolution differences. High spatial resolution 2D images of non-passivated and Ar/CO_2 sample are included in the SI with a 500 µm × 500 µm analysis region (see Fig. S12 and S13).

ToF-SIMS data analysis

ToF-SIMS data was analyzed using SurfaceLab 7.3 software (IONTOF GmbH, Münster, Germany). Mass spectra were calibrated with m/z^- 14.02 CH_2^-, m/z^- 31.99 O_2^-, m/z^- 43.97 SiO^-, m/z^- 75.96 SiO_3^-, m/z^- 160.89 $SiCs^-$ in the negative mode and m/z^+ 23.01 LiO^+, m/z^+ 29.03 CH_3N^+, m/z^+ 38.96 K^+, m/z^+ 53.04 $C_4H_5^+$, m/z^+ 176.88 $SiOCs^+$ in the positive mode. The calibration, spectral analysis, and 2D/3D image reconstructions were performed in the SurfaceLab software. The ToF-SIMS depth profiling and mass spectral data were exported as ASCII files and plotted using Origin Pro 2023 (OriginLab, Northampton, Massachusetts, USA). The "search compounds" function of SurfaceLab was used to identify peaks, and published literature references were also used in peak identification.

Results and discussion

ToF-SIMS spectral analysis identifies lithium–silicon/silicate alloys

The possible peak identifications are shown in Tables 1 and 2 for the negative ion mode. Peaks with a mass deviation of 65 ppm or less are included. Additional peak identifications are provided in Tables S1–S6.

Lithium deposition *via* the thermal evaporation process onto a Si-based electrode leads to the migration of lithium into the bulk of the electrode forming amorphous Li_xSi_y alloys through solid state diffusion due to the high temperatures (>400 °C) of the incoming lithium and the large thermodynamic driving force for lithium alloying reactions with silicon. ToF-SIMS spectral analysis was used to help validate the effectiveness of thermal evaporation as a prelithiation method by identifying lithium–silicon and lithium–silicate alloys.

Fig. 2 shows the ToF-SIMS spectral results within mass range m/z^- 50–100 of silicon-based composite electrodes exposed to an Ar/CO_2 environment after prelithiation (a), an inert Ar gas environment after prelithiation (b), and control electrode with no prelithiation (c). The strong presence of silicon and carbon-based compounds in the spectral plots verify the silicon–carbon electrode composition. Fig. 2 highlights spectral peak areas from m/z^- 50–100 showing m/z^- 62.97 $LiSi_2^-$, m/z^- 66.98 $LiSiO_2^-$, and m/z^- 82.98 $LiSiO_3^-$ peaks present in the samples. This mass range shows formation of Li_xSi_y alloys and $Li_xSi_yO_z$ phases.

Table 1 Peak identification of the prelithiated anode exposed to inert, Ar gas environment in the negative ion mode

m/z^-_{obs} [a]	m/z^-_{theo} [b]	ΔM (ppm)[c]	Species	Assignment	Ref.
7.0164	7.0166	25.414	Li^-	Lithium	47
12.0005	12.0005	6.6797	C^-	Carbon	47
27.9788	27.9775	45.8948	Si^-	Silicon	48
34.9928	34.9935	20.4321	$LiSi^-$	Li_xSi_y alloy	This work
50.9897	50.9884	25.9407	$LiSiO^-$	$Li_xSi_yO_z$ phase	This work
62.9712	62.9704	12.0339	$LiSi_2^-$	Li_xSi_y alloy	This work
66.986	66.9833	40.1563	$LiSiO_2^-$	$Li_xSi_yO_z$ phase	This work
78.967	78.9653	21.8536	$LiSi_2O^-$	$Li_xSi_yO_z$ phase	This work
82.982	82.9782	45.3584	$LiSiO_3^-$	$Li_xSi_yO_z$ phase	This work
90.9477	90.9473	4.1176	$LiSi_3^-$	Li_xSi_y alloy	This work
97.0131	97.0102	30.0005	$Li_3SiO_3^-$	$Li_xSi_yO_z$ phase	This work

m/z^- represents the mass-to-charge ratio for negatively charged ions. [a] $m/z^-_{obs.}$ represents the observed mass to charge ratio. [b] $m/z^-_{theo.}$ represents the theoretical mass to charge ratio. [c] ΔM: $\Delta M = 10^6 \times (m/z^-_{obs.} - m/z^-_{theo.})/m/z^-_{theo.}$ (expressed in ppm).[49] Peak identification are possibilities identified by SurfaceSpectra software and cross-referenced to literature.

Table 2 Peak identification of the prelithiated anode exposed to Ar/CO_2 gas environment in the negative ion mode

m/z^-_{obs} [a]	m/z^-_{theo} [b]	ΔM (ppm)[c]	Species	Assignment	Ref.
7.0166	7.0166	0.1463	Li^-	Lithium	47
12.0007	12.0005	9.7492	C^-	Carbon	47
27.9785	27.9775	37.0930	Si^-	Silicon	48
34.9931	34.9935	11.1301	$LiSi^-$	Li_xSi_y alloy	This work
50.9907	50.9884	46.1284	$LiSiO^-$	$Li_xSi_yO_z$ phase	This work
62.9720	62.9704	25.4692	$LiSi_2^-$	Li_xSi_y alloy	This work
66.9891	66.9833	86.9175	$LiSiO_2^-$	$Li_xSi_yO_z$ phase	This work
78.9689	78.9653	45.9164	$LiSi_2O^-$	$Li_xSi_yO_z$ phase	This work
82.9836	82.9782	64.3833	$LiSiO_3^-$	$Li_xSi_yO_z$ phase	This work
90.9488	90.9473	16.2503	$LiSi_3^-$	Li_xSi_y alloy	This work
97.0165	97.0102	64.6421	$Li_3SiO_3^-$	$Li_xSi_yO_z$ phase	This work
120.0143	120.0212	56.9265	$Li_4SiO_4^-$	$Li_xSi_yO_z$ phase	This work

m/z^- represents the mass-to-charge ratio for negatively charged ions. [a] $m/z^-_{obs.}$ represents the observed mass to charge ratio. [b] $m/z^-_{theo.}$ represents the theoretical mass to charge ratio. [c] ΔM: $\Delta M = 10^6 \times (m/z^-_{obs.} - m/z^-_{theo.})/m/z^-_{theo.}$ (expressed in ppm).[49] Peak identification are possibilities identified by SurfaceSpectra software and cross-referenced to literature.

The control sample, depicted in Fig. 2c, with no prelithiation has negligible or undetected Li^-, $LiSi_2^-$, $LiSiO_2^-$, and $LiSiO_3^-$ peaks in the negative mode. Spectral comparison in the positive ion mode of Ar/CO_2 environment after prelithiation and no prelithiation samples is included in the Fig. S5–S7. The prelithiation under Ar/CO_2 gas environment, Fig. 2a, shows higher intensity values for $Si_xO_y^-$, $Li_xSi_y^-$, and $Li_xSi_yO_z$ compounds compared to prelithiation under Ar gas environment (Fig. 2b). Species such as $LiSi_2^-$, $LiSiO_2^-$, and $LiSiO_3^-$ show intensity values of 90 024, 270 280, and 880 891, respectively, for Ar/CO_2 environment which are increased from the same species observed in the inert Ar environment which show intensity values of 89 156, 172 770, and 312 155 for $LiSi_2^-$, $LiSiO_2^-$, and $LiSiO_3^-$ respectively. However, the formation of silicon carbide SiC_2^- has a higher intensity value, 1 022 745, in the Ar environment compared to the Ar/CO_2 environment intensity value of 428 892. More counts of silicon carbide could indicate shallow lithium passivation into the electrode or reactivity of the Si and carbon within the electrode or the reaction with silicon during milling with propylene carbonate to form small domains of Si–C. In contrast, the high intensities of the lithium–silicates and lower SiC_2^- signal could indicate better conditions for lithium–silicate formation leading to higher stability electrodes. The lithium–silicon and lithium–silicate alloys observed within the ToF-SIMS spectra provide chemical information, suggesting the penetration of lithium into the silicon electrode. Formation of Li_xSi_x alloys may correlate with Li evaporation thickness.[37]

The atmospheric conditions for sample preparation can provide influence on the chemical reaction formation of the Li_xSi_y and $Li_xSi_yO_z$. CO_2 has been shown to have reaction combination properties, influencing side reactions on anodes.[50–52] The increase in silicate (Si_xO_y) and lithium silicate ($Li_xSi_yO_z$) formation in Fig. 2a could be a direct result from the CO_2 in the environment. Silicate formation has been found previously on the surface of silicon anodes when introduced to a CO_2 environment, leading to increasing reaction chemistry at the surface of the electrode, when the lithium passivates the surface of the anode.[38,53,54] The presence of the lithium silicates in Fig. 2b is an indicator of O_2 presence within the system, contributing to the formation of $Li_xSi_yO_z$ products or residual oxides from the milling process or stripping O_2 from the CO_2. Mitigation of oxygen presence is difficult to fully remove, but the ion intensity comparison shows that the CO_2

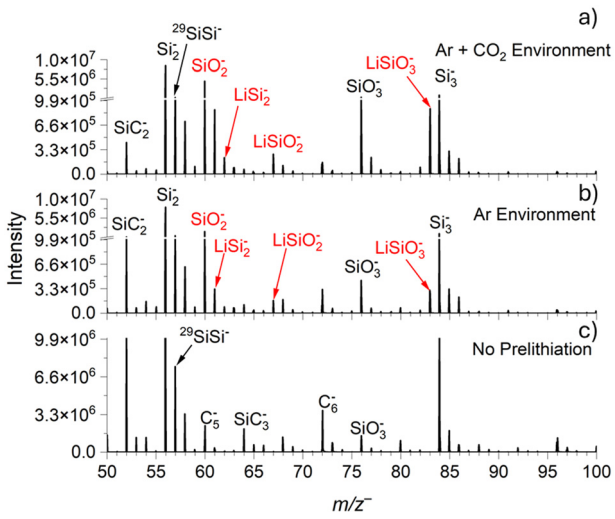

Fig. 2 ToF-SIMS mass spectra collected in negative ion mode within mass range m/z^- 50–100 for prelithiated silicon electrodes housed in Ar + CO_2 environment (a), Ar environment (b), and no prelithiation silicon electrode control sample (c). This mass region shows identifications of $LiSi_2^-$, $LiSiO_2^-$, and $LiSiO_3^-$ peaks found in the prelithiated samples.

is a contributing factor in the increase in peak values observed in Fig. 2a.

ToF-SIMS spectral plots showing mass range m/z^- 0–100 can be found within Fig. S4. The m/z^- 7.01 Li^- peaks confirm the occurrence of prelithiation as lithium, which is typically a positively charged ion. However, identification of m/z^- 7.01 Li^- reflects large amounts of lithium within the anode material, allowing some lithium to have an electronegative charge. Additional positive ion mode spectra in SI provide coorborating evidence, suggesting lithium penetration and formation of Li_xSi alloy formation by utilization of the CsM^+ ionization method.[55–57]

Depth profiling and 2D/3D imaging provide insights into conditions for thermal evaporation

ToF-SIMS molecular imaging reveals 'island-like' lithium deposition pattern actively occurred especially for electrodes placed in purely inert, Ar + CO_2 gas environments. Fig. 3 presents the negative ion mode surface images of four key ions of interest,

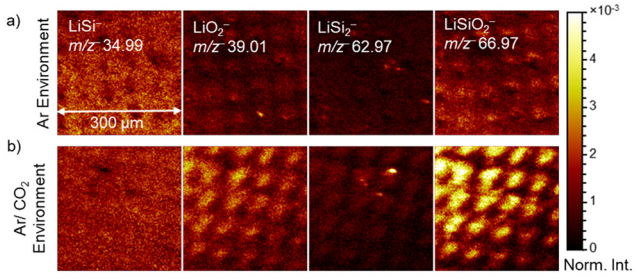

Fig. 3 Normalized SIMS 2D images in the negative ion mode of prelithiated electrodes after exposure to inert Ar gas (a) and Ar/CO_2 gas (b). The analysis area was 300 µm × 300 µm.

namely m/z^- 34.99 $LiSi^-$, m/z^- 39.01 LiO_2^-, m/z^- 62.97 $LiSi_2^-$, and m/z^- 66.97 $LiSiO_2^-$ for prelithiated electrodes after exposure to inert Ar gas (a) and Ar/CO_2 gas (b). Fig. 3 showcases a hatch pattern due to a steel mesh grid which was placed over the silicon electrode to protect the silicon anode in the analysis region. The lithium deposit areas are congregated in the mesh grid openings, thus producing 'island-like' deposit areas.

Fig. 3a shows lithium silicon alloy ($LiSi^-$/$LiSi_2^-$), lithium oxide (LiO_2^-), and lithium silicate ($LiSiO_2^-$) compound signals across the surface with specific negative regions observed. These negative regions correspond to trapped O_2^- signal. A red, green, blue (RGB) overlay showing the oxygen distribution can be found in the Fig. S8. Fig. 3b showcases the lithium deposition areas as more concentrated within the areas where the mesh grid was absent. The more intense pockets of LiO_2^- and $LiSiO_2^-$ ion signals show the lithium depositing into the holes of the mesh as expected. The results suggest that the CO_2 gas may have helped concentrate the thermal evaporation of lithium. The lithium oxide and lithium silicate phase are more dominate likely due to reactions with the CO_2 gas. Images collected within the positive ion mode can be found in Fig. S9, corroborating the aforementioned results observed within negative ion mode.

Depth profiles were used to examine the depth of lithium penetration into the silicon electrodes after thermal evaporation of lithium. Depth profiles and 3D reconstruction images of the analysis area for silicon electrodes in Ar/CO_2 and inert Ar environments are reported in Fig. 4. Depth profiles in positive and negative mode of the no prelithiation silicon electrode control can be found in Fig. S10. The depth profiles reached a total depth of 400 nm after a total sputter time of 2500 s, indicating a sputtering rate of 0.16 nm s^{-1} for each sample. Fig. 4a and c present the depth profiles which highlight thermal evaporation's ability to effectively disperse lithium throughout the electrodes as we can track distributions of molecules, such as Li^-, Si^-, $LiSi^-$, $LiSi_2^-$, $LiSiO_2^-$, and LiO_2^-.

Fig. 4a corresponds to the prelithiated electrode material exposed to inert Ar gas environment, while Fig. 4c corresponds to the prelithiated electrode material exposed to an Ar/CO_2 gas environment. Expectedly, the highest concentration of lithium is found on the surface of the electrodes. The increased intensities of both the Li^- and LiO_2^- depth profile lines in Fig. 4a and c followed by the slowly increasing growth of Si^- intensities show that a layer of lithium forms atop the silicon electrodes where the steel mesh was placed, creating pockets. Despite the layer growth and steel mesh's restricted areas of deposition, lithium is still dispersed throughout the electrodes as the depth profiling and 3D image data highlight. The formed lithium layer due to use of steel mesh shows restrictions the lithium from randomly diffusing throughout the sample electrodes.

The Ar/CO_2 also has lithium spread laterally across the surface possibly due to CO_2 gas or surface alteration, after the mesh was removed prior to ToF-SIMS analysis. These pockets are observed when examining other ion species (*i.e.*, Li_2O).

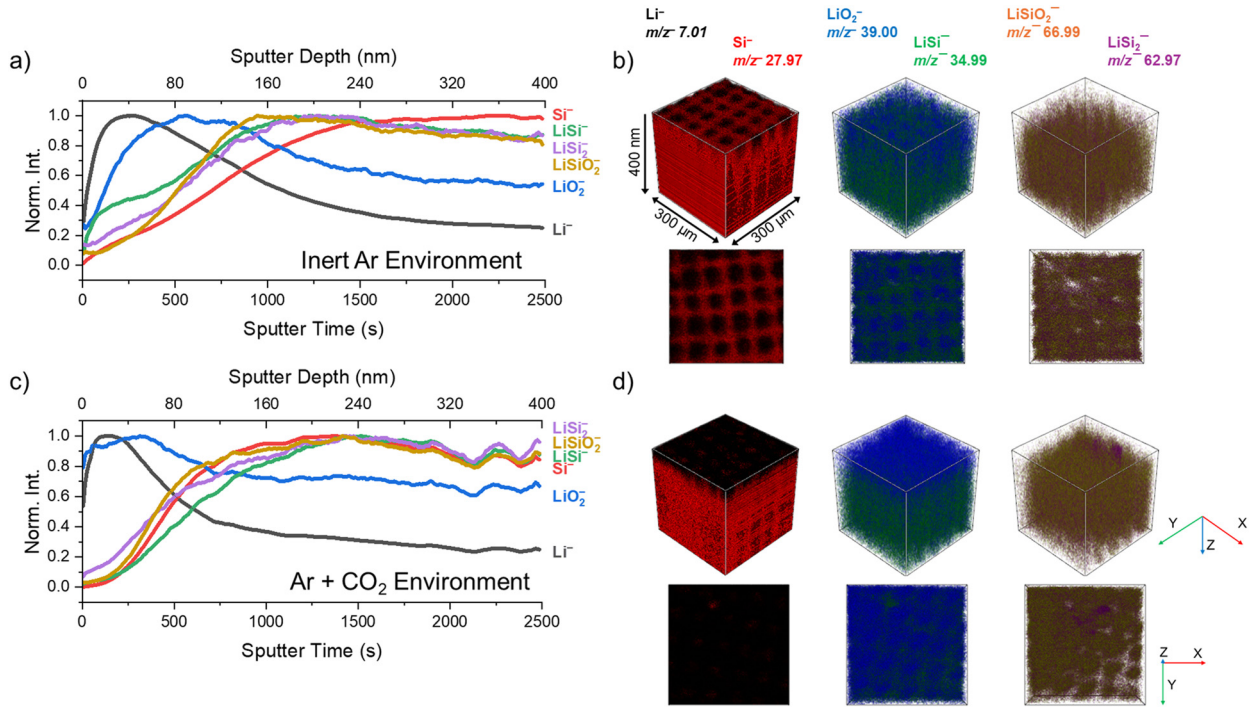

Fig. 4 ToF-SIMS depth profiles (a and c) and overlaying reconstructed 3D SIMS images (b and d) of the prelithiated electrode materials after exposure to an inert Ar gas environment (a and b) and an Ar/CO_2 gas environment (c and d) in the negative ion mode. Total sputtering depth was 400 nm. Sputtering done at 0.16 nm s^{-1}. The same colors are used for identified ions in the depth profiles and 3D images. 3D reconstructions were binned by 4 pixels in *XY* and 4 pixels in *Z*.

Our mass spectral imaging results substantiate the steel mesh as a beneficial addition to the thermal evaporation process because it reduces the electrodes' strain and volumetric expansion while still enabling effective prelithiation to occur. Fig. 4c and d show observations of a high intensity in lithium followed by a steady decrease as well as a layer of lithium atop the surface for the prelithiated anode under Ar/CO_2 conditions. The point at which the Li^-/Si^- cross indicates the depth of the anode material where the interface of the anode and the thermal evaporated lithium becomes more important. Under Ar/CO_2 conditions, this interface section arrives at 82.4 nm in depth whereas this interface occurs at 140 nm in depth for the inert Ar conditions. However, lithium overall depletes similarly under both conditions. Chemical reaction under Ar/CO_2 conditions allows the formation of lithium silicon (Li_xSi_y) and lithium silicate ($Li_xSi_yO_z$) to form closer to the surface and remain at high intensity levels throughout the sample. Formation of Li_xSi_y and $Li_xSi_yO_z$ species closer to the surface can potentially help H_2 storage.[58]

Visualization of the lithium incorporation into the silicon electrode material after prelithiation is made possible by 3D reconstruction as depicted in Fig. 4b, inert Ar gas environment, and Fig. 4d, Ar/CO_2 gas environment. Both Fig. 4b and d provide visual evidence of dense distributions of Li_xSi_y and $Li_xSi_yO_z$ molecular signals. We observe specific channels of lithium penetration, as shown by Li^- in black and $LiSi^-$ shown in green, where the lithium stayed within the path designated by the mesh grid. We also show that the LiO_2^- distribution is more significant for the inert Ar/CO_2 gas environment *versus* the LiO_2^- for the Ar gas environment, the latter leaving a uniform layer at the top of the material. This is likely due to lithium readily reacting with the environment to form an oxide layer. The oxide layer stays mostly at the surface according to the depth profile and reconstructed 3D images as shown in Fig. 4c and d. $LiSi_2^-$ is a likely fragment from a larger Li_xSi_y molecule. Positive mode depth profiles and 3D images of the inert Ar gas environment and an Ar/CO_2 gas environment can be found in Fig. S11.

Lithium silicate tends to form over lithium silicon alloys

Although ToF-SIMS is not used to precisely quantify the degrees to which certain compounds form, our results suggest that both Li_xSi_y alloy and $Li_xSi_yO_z$ silicate compounds form in more readily under Ar/CO_2 conditions. Fig. 4 highlights LiO_2^- and $LiSiO_2^-$ having greater surface presence in the Ar/CO_2 environment, most likely stemming from the presence of the CO_2 decomposing into carbon and oxygen compounds. Each passivation environment shows similar intensities for $LiSi^-$ and $LiSi_2^-$ throughout the samples. The stronger presence of $Li_xSi_yO_z$ silicates is further substantiated by the identification of compounds, such as $Li_3SiO_3^+$, $LiSiO^+$, and $Li_3SiO_2^+$, compared to $LiSi^+$ and Li_2Si^+ seen in the positive mode depth profiles (Fig. S11) of the same samples. The greater number of silicate compounds existence at larger or similar intensities to the

alloying compounds in Fig. 4b and d visually show how densely the most prominent silicate and alloy compounds form throughout the depth profiles. The ΔM mass deviation values for our Li_xSi_y alloys and $Li_xSi_yO_z$ silicates range up to ±87 ppm for the negative mode (Tables 1 & 2) and ±68 ppm for the positive mode (Tables S4 and S5). These mass deviation values along with many of these compounds not being found in the non-prelithiated samples suggest our peak identification is reliable.

Two recent studies reported that forming $Li_xSi_yO_z$ silicates contributed to improved capacity retention and ICE in prelithiated silicon electrodes.[33,34] Both Bai *et al.*[33] and Bhat *et al.*[34] analyzed prelithiated silicon electrodes after cycling. According to Bhat *et al.*, having a prelithiation process tailored to only producing $Li_xSi_yO_z$ silicates in an SiO electrode created electrodes with a high ICE value and capacity retention after 200 cycles. Bhat *et al.* highlights that, between the formed silicates, Li_2SiO_3 and $Li_2Si_2O_5$ are the most ideal silicates to be present under moderate prelithiation amounts. They suggest Li_4SiO_4 is a possible sign of over prelithiation. Bai *et al.* found that prelithiated silicon electrodes which grow an SEI layer consisting of Li_2SiO_3, $Li_2Si_2O_5$, and Li_4SiO_4 are more stable and conductive compared to non prelithiated silicon electrodes that normally form Li_2CO_3 and LiF SEI compounds after cycling. Although our ToF-SIMS results did not show Li_2CO_3 or $Li_2Si_2O_5$ compounds in the uncycled samples, these desirable silicates may form due to cycling. Our SIMS analyses suggest thermal evaporation may be effective in producing stable electrodes.

The silicon for the anode is prepared by milling with propylene carbonate to functionalize the surface. During the milling process, the Si breaks down and forms Si–C bonds at the surface. This covalent bonding is likely the reason behind the SiC observation.[59] The increase in SiC_2^- peak observed for the Ar environment and no-prelithiation environment in Fig. 2 is due to the lack of Li_xSi_y and $Li_xSi_yO_z$ formation. The Ar/CO_2 environment sample has these molecules closer to the surface, potentially reducing the amount of ionizable SiC at the surface. Additional evidence is depicted in Fig. 4. Li_xSi_y and $Li_xSi_yO_z$ molecules are detected at approximately 80 nm in the Ar/CO_2 environment depth profiles compared to 140 nm in those of the inert Ar environment. Formation of the Li_xSi_y and $Li_xSi_yO_z$ molecules closer to the surface may have impact on the cycling stability and specific capacity of the anodes.

Fig. 5 shows the specific capacity comparison after cycling for Ar/CO_2 and Ar only anode. The result reveals a 14.8% increase in specific capacity when cycling after SEI formation. This is possibly due to the fact that available lithium reacts with surface molecules before cycling of the Ar-only anode. In contrast, CO_2 may passivate lithium, allowing for the formation of the Li_xSi_y and $Li_xSi_yO_z$ molecules. When preparing these anodes, CAMP Si (2.0 mAh cm^{-2}) was paired with NMC 811 to give a N/P of 0.8. The electrolyte was GenF3 and separator was Celgard 2325.[60] Cycling was done at a C/20 rate for 3 cycles to enable SEI formation before subsequent C/3 cycling. Identification of the Li_xSi_y and $Li_xSi_yO_z$ molecules closer to the surface and the higher specific capacity observed for the Ar/CO_2 anode provide strong evidence for a more stable Si anode.

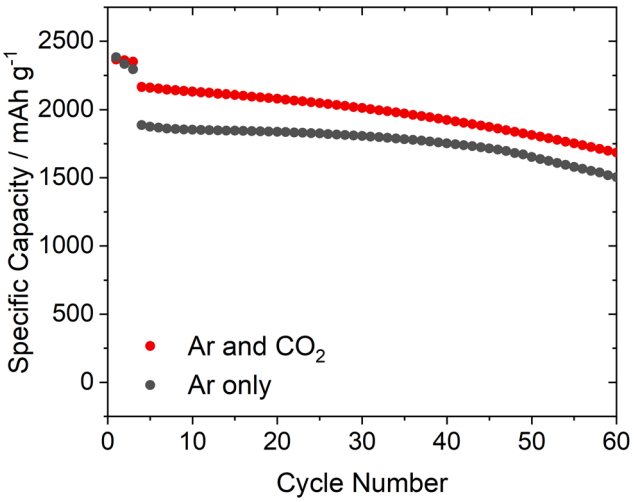

Fig. 5 Anode cycling *versus* specific capacity for Ar/CO_2 anode and Ar only anode, indicating a 14.8% increase in specific capacity observed when cycling after solid-electrolyte interphase formation.

Conclusions

Through ToF-SIMS analysis and particularly its visual recreations, thermal evaporation was shown to uniformly prelithiate electrode materials with a steel mesh confining the lithium deposition to 'pockets'. The prelithiated samples had strong lithium presence throughout their depth profiles and visually showed homogeneous dispersions of interphase Li_xSi_y and $Li_xSi_yO_z$ compounds. Restricting prelithiation to specific channels still allows uniform distributions of lithium while alleviating the electrodes' volumetric expansion from prelithiation. Our results suggest that future thermal evaporation prelithiating process should incorporate steel meshes or similar confining tools to mitigate the volumetric expansion. Our results also suggest that Ar/CO_2 environment may have helped create a prosperous environment for Li_xSi_y alloy formation. Further experiments are necessary to determine which other gas environments could provide beneficial results.

ToF-SIMS proves to be an effective characterization tool for studying prelithiation dynamics. Our ToF-SIMS results provided a unique angle for evaluating the viability of prelithiation *via* thermal evaporation. Our 2D images were able to spatially resolve specific features like the 'pockets' where prelithiation occurred and where silicon was less impacted under the grids. We also identified the formation of various $Li_xSi_yO_z$ silicates and Li_xSi_y alloy compounds and found that the electrodes contained likely higher concentrations of $Li_xSi_yO_z$ silicates overall. Since these silicates are preferable for forming more stable solid electrolyte interphase, our results suggest that thermal evaporation could be an effective prelithiation method for silicon anodes. The passivation depths are com-

parable between the two environments. However, the depth profiling data suggests that the Ar/CO_2 passivation forms alloy and oxide phases closer to the surface and increases the abundance of Li_xSi_y alloy and $Li_xSi_yO_z$ phase, which creates a more stable anode. Additional ToF-SIMS studies should be done on cycled electrodes to analyze performance, SEI layer composition, and electrode composition after cycling. Better understandings of ideal prelithiation levels, alloy concentrations, and silicate concentrations would help guide process modifications.

Author contributions

G. D. P. provided data curation, formal analysis, investigation, methodology, validation, visualization, writing – original draft preparation, and writing – review and editing; I. M. provided formal analysis, visualization, writing – original draft preparation; A. L. M. provided conceptualization, methodology, resources, writing – review and editing; G. M. V. provided conceptualization, project administration, resources, writing – review and editing; X. Y. Y. provided conceptualization, funding acquisition, investigation, project administration, resources, software, supervision, validation, writing – review and editing.

Conflicts of interest

There are no conflicts to declare.

Data availability

The authors declare that the data supporting the findings of this study are available within the paper and its supplementary information (SI). Supplementary information is available. See DOI: https://doi.org/10.1039/d5nr05002b.

Should any raw data files be needed in another format they are available from the corresponding author upon reasonable request.

Acknowledgements

Gabriel D. Parker was funded by the Graduate Research Program at ORNL (GRO) internship program at the Oak Ridge National Laboratory (ORNL). Ivan Matyushov was funded by ORNL Science Undergraduate Laboratory Internship (SULI) program and the Department of Energy Renew Program (Project ERAT821) for supporting his visit at ORNL. Dr Xiao-Ying Yu is indebted to the support by the strategic Laboratory Directed Research and Development (LDRD, project 11167) of the Physical Sciences Directorate of the Oak Ridge National Laboratory (ORNL). ToF-SIMS data collection was performed using the Center for Nanophase Materials Sciences (CNMS) user proposal (CNMS2024-B-02747). A portion of this work (prelithiation – ALM, GMV) was supported by the United States Department of Energy's Office of Energy Efficiency and Renewable Energy, Vehicle Technologies Office, Silicon Consortium Program, led by Carine Steinway, Nicolas Edison, Thomas Do, and Brian Cunningham and directed by Anthony Burrell.

This manuscript has been authored by UT-Battelle, LLC under contract no. DE-AC05-00OR22725 with the U.S. DOE. The United States Government retains and the publisher, by accepting the article for publication, acknowledges that the United States Government retains a non-exclusive, paid-up, irrevocable, worldwide license to publish or reproduce the published form of this manuscript, or allow others to do so, for United States Government purposes. The DOE will provide public access to these results of federally sponsored research in accordance with the DOE Public Access Plan (https://energy.gov/downloads/doe-public-access-plan).

References

1 H. Zhang, Y. Yang, D. Ren, L. Wang and X. He, *Energy Storage Mater.*, 2021, **36**, 147–170.
2 K. Feng, M. Li, W. Liu, A. G. Kashkooli, X. Xiao, M. Cai and Z. Chen, *Small*, 2018, **14**, 1702737.
3 Y. J. Choi, Y. S. Lee, J. H. Kim and J. S. Im, *Materials*, 2023, **16**, 6896.
4 A. S. Aricò, P. Bruce, B. Scrosati, J.-M. Tarascon and W. van Schalkwijk, *Nat. Mater.*, 2005, **4**, 366–377.
5 L. Y. Beaulieu, T. D. Hatchard, A. Bonakdarpour, M. D. Fleischauer and J. R. Dahn, *J. Electrochem. Soc.*, 2003, **150**, A1457.
6 T. Yoon, C. C. Nguyen, D. M. Seo and B. L. Lucht, *J. Electrochem. Soc.*, 2015, **162**, A2325.
7 F. Wang, B. Wang, J. Li, B. Wang, Y. Zhou, D. Wang, H. Liu and S. Dou, *ACS Nano*, 2021, **15**, 2197–2218.
8 B. Hu, S. Jiang, I. A. Shkrob, J. Zhang, S. E. Trask, B. J. Polzin, A. Jansen, W. Chen, C. Liao, Z. Zhang and L. Zhang, *J. Power Sources*, 2019, **416**, 125–131.
9 Z. Li, W. Tang, Y. Yang, G. Lai, Z. Lin, H. Xiao, J. Qiu, X. Wei, S. Wu and Z. Lin, *Adv. Funct. Mater.*, 2022, **32**, 2206615.
10 J. Zhang, J. Sun, Y. Zhao, Y. Su, X. Meng, L. Yan and T. Ma, *J. Colloid Interface Sci.*, 2023, **649**, 977–985.
11 R. Zhu, S. Liu, T. Li and D. Yang, *ChemElectroChem*, 2024, **11**, e202400326.
12 N. Liu, L. Hu, M. T. McDowell, A. Jackson and Y. Cui, *ACS Nano*, 2011, **5**, 6487–6493.
13 A. Rezqita, A.-R. Kathribail, J. Kahr and M. Jahn, *J. Electrochem. Soc.*, 2019, **166**, A5483.
14 T. Eguchi, R. Sugawara, Y. Abe, M. Tomioka and S. Kumagai, *Batteries*, 2022, **8**, 49.
15 Y. Zhang, B. Wu, J. Bi, X. Zhang, D. Mu, X. Y. Zhang, L. Zhang, Y. Xiao and F. Wu, *Carbon Energy*, 2024, **6**, e480.
16 Y. Shen, J. Zhang, Y. Pu, H. Wang, B. Wang, J. Qian, Y. Cao, F. Zhong, X. Ai and H. Yang, *ACS Energy Lett.*, 2019, **4**, 1717–1724.

17 X. Zhang, H. Qu, W. Ji, D. Zheng, T. Ding, D. Qiu and D. Qu, *J. Power Sources*, 2020, **478**, 229067.
18 M.-Y. Yan, G. Li, J. Zhang, Y.-F. Tian, Y.-X. Yin, C.-J. Zhang, K.-C. Jiang, Q. Xu, H.-L. Li and Y.-G. Guo, *ACS Appl. Mater. Interfaces*, 2020, **12**, 27202–27209.
19 J. Shi, C.-C. Su, R. Amine, X. Wu, P. Lamp, F. Maglia, R. Jung and K. Amine, *ACS Appl. Mater. Interfaces*, 2023, **15**, 26710–26717.
20 P. Bärmann, M. Mohrhardt, J. E. Frerichs, M. Helling, A. Kolesnikov, S. Klabunde, S. Nowak, M. R. Hansen, M. Winter and T. Placke, *Adv. Energy Mater.*, 2021, **11**, 2100925.
21 W. He, H. Xu, Z. Chen, J. Long, J. Zhang, J. Jiang, H. Dou and X. Zhang, *Nano-Micro Lett.*, 2023, **15**, 107.
22 P. Lai, C. Liu, Z. Sun and Z. Zhang, *Solid State Ion.*, 2023, **403**, 116415.
23 X. Li, C. Bian, J. Zhang, J. Hong, R. Fu, X. Zhou, Z. Liu and G. Shao, *ACS Appl. Energy Mater.*, 2023, **6**, 8919–8928.
24 Y. Domi, H. Usui, D. Iwanari and H. Sakaguchi, *J. Electrochem. Soc.*, 2017, **164**, A1651.
25 P. Bärmann, M. Diehl, L. Göbel, M. Ruttert, S. Nowak, M. Winter and T. Placke, *J. Power Sources*, 2020, **464**, 228224.
26 H. Chen, Y. Yang, D. T. Boyle, Y. K. Jeong, R. Xu, L. S. de Vasconcelos, Z. Huang, H. Wang, H. Wang, W. Huang, H. Li, J. Wang, H. Gu, R. Matsumoto, K. Motohashi, Y. Nakayama, K. Zhao and Y. Cui, *Nat. Energy*, 2021, **6**, 790–798.
27 M. Gautam, G. K. Mishra, A. Ahuja, S. Sau, M. Furquan and S. Mitra, *ACS Appl. Mater. Interfaces*, 2022, **14**, 17208–17220.
28 S.-Y. Ham, E. Sebti, A. Cronk, T. Pennebaker, G. Deysher, Y.-T. Chen, J. A. S. Oh, J. B. Lee, M. S. Song, P. Ridley, D. H. S. Tan, R. J. Clément, J. Jang and Y. S. Meng, *Nat. Commun.*, 2024, **15**, 2991.
29 G. M. Overhoff, R. Nölle, V. Siozios, M. Winter and T. Placke, *Batteries Supercaps*, 2021, **4**, 1163–1174.
30 B. Stumper, A. Mayr, K. Mosler, J. Kriegler and R. Daub, *J. Electrochem. Soc.*, 2024, **171**, 059002.
31 B. Stumper, O. Wittmann, F. Diller, S. Stock and R. Daub, *J. Electrochem. Soc.*, 2024, **171**, 120510.
32 X.-Y. Yue, Y.-X. Yao, J. Zhang, S.-Y. Yang, Z. Li, C. Yan and Q. Zhang, *Adv. Mater.*, 2022, **34**, 2110337.
33 S. Bai, W. Bao, K. Qian, B. Han, W. Li, B. Sayahpour, B. Sreenarayanan, D. H. S. Tan, S.-y. Ham and Y. S. Meng, *Adv. Energy Mater.*, 2023, **13**, 2301041.
34 A. Bhat, P. Sireesha, Y.-S. Chen and Y.-S. Su, *ChemElectroChem*, 2022, **9**, e202200772.
35 E. Adhitama, F. Dias Brandao, I. Dienwiebel, M. M. Bela, A. Javed, L. Haneke, M. C. Stan, M. Winter, A. Gomez-Martin and T. Placke, *Adv. Funct. Mater.*, 2022, **32**, 2201455.
36 E. Adhitama, M. M. Bela, F. Demelash, M. C. Stan, M. Winter, A. Gomez-Martin and T. Placke, *Adv. Energy Mater.*, 2023, **13**, 2203256.
37 A. L. Musgrove, K. L. Browning, R. L. Sacci, A. Ullman, H. M. Meyer III, K. Musgrove, J. Quinn, S. Möller, M. Finsterbusch and G. M. Veith, *Energy Fuels*, 2025, **39**, 4968–4982.
38 Y.-S. Su, K.-C. Hsiao, P. Sireesha and J.-Y. Huang, *MDPI Batteries*, 2022, **8**, 8010002.
39 J. Sun, L. Huang, G. Xu, S. Dong, C. Wang and G. Cui, *Mater. Today*, 2022, **58**, 110–118.
40 T. Lombardo, F. Walther, C. Kern, Y. Moryson, T. Weintraut, A. Henss and M. Rohnke, *J. Vac. Sci. Technol., A*, 2023, **41**, 053207.
41 L. E. Strange, M. H. Engelhard, C. D. Easton, J.-M. Kim and D. R. Baer, *Surf. Interface Anal.*, 2023, **55**, 715–729.
42 S. Zhou, K. Liu, Y. Ying, L. Chen, G. Meng, Q. Zheng, S.-G. Sun and H.-G. Liao, *Curr. Opin. Electrochem.*, 2023, **41**, 101374.
43 C. Fang, J. Lau, D. Hubble, P. Khomein, E. A. Dailing, Y. Liu and G. Liu, *Joule*, 2021, **5**, 415–428.
44 J. J. A. Kreissl, J. Petit, R. Oppermann, P. Cop, T. Gerber, M. Joos, M. Abert, J. Tübke, K. Miyazaki, T. Abe and D. Schröder, *ACS Appl. Mater. Interfaces*, 2021, **13**, 35625–35638.
45 Y. Feng, B. M. Koo, A. Seyeux, J. Światowska, C. Henry de Villeneuve, M. Rosso and F. Ozanam, *ACS Appl. Mater. Interfaces*, 2022, **14**, 35716–35725.
46 Y. Yamagishi, H. Morita, Y. Nomura and E. Igaki, *J. Phys. Chem. Lett.*, 2021, **12**, 4623–4627.
47 N. Gauthier, C. Courrèges, J. Demeaux, C. Tessier and H. Martinez, *Appl. Surf. Sci.*, 2020, **501**, 144266.
48 V. A. Brown, D. A. Barrett, P. N. Shaw, M. C. Davies, H. J. Ritchie, P. Ross, A. J. Paul and J. F. Watts, *Surf. Interface Anal.*, 1994, **21**, 263–273.
49 X.-Y. Yu, C. Yang, J. Gao, J. Xiong, X. Sui, L. Zhong, Y. Zhang and J. Son, *Front. Chem.*, 2023, **11**, 1253685.
50 E. J. Hopkins, S. Frisco, R. T. Pekarek, C. Stetson, Z. Huey, S. Harvey, X. Li, B. Key, C. Fang, G. Liu, G. Yang, G. Teeter, N. R. Neale and G. M. Veith, *J. Electrochem. Soc.*, 2021, **168**, 030534.
51 L. J. Krause, V. L. Chevrier, L. D. Jensen and T. Brandt, *J. Electrochem. Soc.*, 2017, **164**, A2527–A2533.
52 E. Arca, G. M. Veith, R. Satish, T. Lin, G. Teeter and R. Kostecki, *J. Phys. Chem. C*, 2022, **126**, 14058–14066.
53 K. Wang, Z. Yin and P. Zhao, *Ceram. Int.*, 2016, **42**, 2990–2999.
54 Y. Xiao, G. Wang, S. Zhou, Y. Sun, Q. Zhao, Y. Gong, T. Lu, C. Luo and K. Yan, *Electrochim. Acta*, 2017, **223**, 8–20.
55 J. Brison and L. Houssiau, *Nucl. Instrum. Methods Phys. Res., Sect. B*, 2007, **259**, 984–988.
56 J. Brison, R. G. Vitchev and L. Houssiau, *Nucl. Instrum. Methods Phys. Res., Sect. B*, 2008, **266**, 5159–5165.
57 Y. Kudriavtsev, R. Asomoza, M. Mansurova, L. A. Perez and V. M. Korol', *Tech. Phys.*, 2013, **58**, 735–743.
58 K. Doi, S. Hino, H. Miyaoka, T. Ichikawa and Y. Kojima, *J. Power Sources*, 2011, **196**, 504–507.
59 K. G. Araño, B. L. Armstrong, E. Boeding, G. Yang, H. M. Meyer III, E. Wang, R. Korkosz, K. L. Browning, T. Malkowski, B. Key and G. M. Veith, *ACS Appl. Mater. Interfaces*, 2023, **15**, 10554–10569.
60 A. L. Musgrove, A. Verma, M.-T. F. Rodrigues, C. I. McDaniel, D. P. Abraham, S. Lam, A. Colclasure, A. Singh, B. L. Armstrong and G. M. Veith, *Adv. Mater. Technol.*, 2026, **11**, e02088.